nature nanotechnology

Article

https://doi.org/10.1038/s41565-026-02182-5

Anomalous ultrafast lithium-ion transport through boron nitride nanotube membranes

Received: 16 October 2024

Accepted: 10 April 2026

Published online: 12 June 2026

Check for updates

Semih Cetindag[1], Aaditya Pendse[2], Pavel Rehak[3], Volodymyr Koverga[2,4], Selva C. Selvaraj[2,4], Naveen K. Dandu[2,4], Roya Jafari[3], Richard J. Castellano[1,5], Matthew Howard[1], Kun Wang[2], Joshua Yi[1,6], Robert F. Praino[5], Liping Liu[1,7], Anh T. Ngo[2,4], Petr Kral[2,3] ✉, Sangil Kim[2] ✉ & Jerry W. Shan[1] ✉

Here we studied the aqueous transport of different alkali-metal ions in charged boron nitride nanotubes (BNNTs) and compared the results with those obtained in carbon nanotubes, using macroscopic, vertically aligned nanotube membranes at densities up to 10^7 pores cm^{-2}. Our study reveals that ion transport in 3- and 12-nm-diameter charged BNNTs is fundamentally different from that in either carbon nanotubes of a similar size, or two-dimensional boron nitride nanochannels. We find two unexpected transport phenomena: ultrafast, cation-selective diffusion that exceeds Fickian diffusion up to 31-fold; and preferentially enhanced transport rates for Li^+ over other alkali-metal ions (K^+ and Na^+) that are opposite to the ordering of their mobilities in bulk solution. We show that the overall fast transport of cations is due to diffusio-osmotic surface transport, while the preferentially enhanced transport of Li^+ is believed to result from ion-specific interactions with the charged BNNTs. As a result of enhanced and cation-selective transport, the BNNT membranes produced per-pore osmotic-power densities up to 15,300 W m^{-2} in a 1 mM:1 M LiCl concentration gradient at pH 11. The energy-conversion efficiency approached the theoretical limit of 50% at pH 5.5. As a demonstration, we power a calculator, watch and light-emitting diode using 1-cm^2 BNNT membranes in a salinity gradient. The unusual transport phenomena in BNNTs, as well as the flexible and scalable membrane-fabrication process, may enable ion-selective nanotube membranes optimized for lithium recovery, 'blue' osmotic energy and other separation and energy-conversion processes.

The rapid and selective transport of ions through nanopores is central to biological systems, as well as a variety of energy-conversion and molecular-separation processes. A number of remarkable ion-transport phenomena have been observed in nanopores, nanotubes and nanochannels, including exquisite ion selectivity[1–3], complete ion exclusion[4], enhanced mobility[5–7] and osmotic-power generation[8,9]. Pioneering work by Siria et al. has shown that, in individual charged boron nitride (BN) nanotubes (BNNTs) connecting reservoirs with different potassium chloride (KCl) concentrations, a combination of cation selectivity and enhanced transport can generate 'giant' osmotic power from salinity differences[10]. Recent work by Li et al. on few (1–3), short (20–60 nm) BN porins in artificial lipid vesicles has revealed an unusual conductance scaling with KCl concentration, excellent K^+ selectivity that persists to neutral pH and high osmotic powers[11]. However, it is not known how different cations would pass through BNNTs (of relevance, for example, to desalination, batteries or lithium recovery). It is also not clear

A full list of affiliations appears at the end of the paper. ✉e-mail: pkral@uic.edu; sikim@uic.edu; jshan@soe.rutgers.edu

how the ion transport would compare with that in carbon nanotubes nor how the transport would scale up from single or few nanotubes to macroscopic membranes with many BNNT pores.

Here, we report on our observations of anomalous transport of different alkali-metal ions through aligned BNNTs, using macroscopic membranes made with a solution-based, field-assisted method. The ion transport in narrow (3- and 12-nm-diameter) charged BNNTs is found to be fundamentally different from that in either carbon nanotubes of similar size or two-dimensional (2D) BN nanochannels[12,13]. We observe two unexpected transport phenomena: (1) ultrafast, cation-selective diffusion that exceeds Fickian diffusion up to 31-fold and (2) preferentially enhanced transport rates for Li^+ over other alkali-metal ions (K^+ and Na^+) that are opposite to the ordering of their bulk mobilities in solution. We show that the enhanced diffusive transport in charged BNNTs is a result of diffusio-osmosis, with linearly additive transport up to the maximum-tested pore density of ~10^7 nanotubes cm^{-2}. Our study further reveals that the anomalously enhanced transport of driven Li^+ cations appears to arise from species-specific interactions with trapping OH^- groups inside the BNNTs that lead to higher effective axial mobilities. As a result, the BNNT membranes produced per-pore osmotic-power densities up to 15,300 W m^{-2} in a 1 mM:1 M LiCl concentration gradient at pH 11. The maximum energy-conversion efficiencies approached the theoretical limit of 50% for a 1 mM:1 M KCl concentration gradient at pH 5.5 and remained high up to pH 9.5. These unusual transport phenomena, along with the flexible and scalable membrane-fabrication process, may enable ion-selective nanotube membranes optimized for lithium recovery, 'blue' osmotic energy and other separation and energy-conversion processes. As a demonstration, we power a calculator, watch and light-emitting diode (LED) using 1-cm^2 BNNT membranes in a salt concentration gradient.

Results

Fabrication method

We have devised a field-assisted, solution-based method to fabricate macroscopic membranes with vertically aligned (VA) BNNT pores (Fig. 1a). The fabrication method is scalable and provides flexibility in using different types of nanotubes (in powder form) to make membranes. In this work, we aligned BNNTs (3- and 12-nm inner diameter) and carbon nanotubes (CNTs; 3-nm inner diameter) with magnetic and electric fields[14–18], respectively. The BNNTs were decorated with iron-oxide nanoparticles to make them magnetically susceptible and thus alignable by a magnetic field (Fig. 1b,c). By contrast, the CNTs naturally develop an induced electrical dipole under an external electric field as a result of Maxwell–Wagner interfacial polarization[14], so functionalization with nanoparticles was not necessary. The BNNTs or CNTs were then suspended in a liquid urethane prepolymer, aligned and concentrated by the external field and locked in place by in situ ultraviolet (UV) polymerization (Fig. 1d). Plasma etching was used to remove excess polymer and uncap nanotubes, yielding permeable arrays of VA-nanotube embedded in a 4–5-μm-thick polyurethane matrix. We mounted and tested 1-cm^2 samples cut from larger, ~20-cm^2 nanotube arrays. The open-pore densities were up to 6.9×10^6 pores cm^{-2} for the 3-nm BNNT membranes, 2.7×10^5 pores cm^{-2} for the 12-nm BNNT membranes and 1.7×10^5 pores cm^{-2} for the 3-nm CNT membranes. The solution-based, field-assisted membrane-fabrication approach is simple and flexible in the types of nanotubes used. It is also scalable and potentially compatible with roll-to-roll processing[15].

The surface charge of the BN surface can be tuned by adjusting the solution pH, which changes the density of chemi- and physio-sorbed OH^- ions ($BN_3 + H_2O \leftrightarrow BN_3{-}OH^- + H^+$)[19,20]. At low KCl solution molarities, the BNNTs displayed surface-dominated ion transport with a constant conductance that became independent of salt concentration (Fig. 2a,b). Using a model for ionic conductance that accounts for both bulk and surface transport[10],

$$G = \frac{A_{open}}{L_p}\left\{\left[10^3 \mathrm{Lm}^{-3} F\left(\mu_{K^+} + \mu_{Cl^-}\right) C_s\right] + \left[\frac{2\mu_{K^+}|\Sigma|}{R_p}\right]\right\}, \quad (1)$$

the BNNT arrays were deduced from the transport to have surface-charge densities of −170 and −45 mC m^{-2} at pH 11 for the 12-nm and 3-nm BNNTs, respectively. In the above equation, A_{open}, L_p and R_p are the total open area, length and radius of the pores, respectively, while F, μ_{K^+}, μ_{Cl^-}, C_s and Σ are the Faraday constant, mobilities of potassium or chlorine ions, solution concentration and the wall surface-charge density. At pH 7, the BNNT charge densities decreased to −35 and −16 mC m^{-2} for the 12-nm and 3-nm BNNTs, respectively. By contrast, the 3-nm CNTs exhibited negligible surface charge. Instead of showing a constant conductance at low solution molarities, the CNTs followed a power-law $G \sim C_s^{\alpha}$ scaling, with exponent $1/3 < a < 1/2$, that is typical of small-diameter CNTs[3,21,22].

Ion diffusion

Then, we studied diffusive ion transport in the nanotube arrays by immersing the membranes in a salt concentration gradient and measuring their I–V behaviour. For these tests, the high-side molarity C_H was varied, while the low-side molarity C_L was fixed at 1 mM (see the Supplementary Discussion for details). The BNNTs, with their charged surfaces and small diameters, were highly cation selective, while CNTs of the same size were not. The selectivity was quantified as the ratio of cation-to-total ion flux, with the transference number, t^+, calculated from the membrane's diffusion potential, E_{diff}, as[23]

$$t^+ = \frac{J^+}{J^+ + J^-} = \frac{1}{2}\left(\frac{E_{diff}}{\frac{RT}{zF} ln\left(\frac{\gamma_H C_H}{\gamma_L C_L}\right)} + 1\right), \quad (2)$$

where J^+, J^-, $\gamma_{H,L}$, $C_{H,L}$, R, T and z are the cation and anion fluxes, activity coefficient, ion concentration, gas constant, temperature and valence, respectively. The diffusion potential is experimentally found as the difference between the measured open-circuit (zero-current) voltage and the redox potential, that is, $E_{diff} = V_{OC} - E_{redox}$. The subscripts H and L refer to the high- and low-molarity solutions. A transference number of $t^+ = 0$ or 1 implies complete anion or cation selectivity, respectively, while $t^+ = 0.5$ indicates a complete lack of selectivity. Figure 2c,d reveals that the BNNTs possessed excellent K^+ cation selectivity, with t^+ approaching 1. The high selectivity remained constant with increasing C_H, with $t^+ = 0.91$ even for $C_H/C_L = 10^3$ in the 3-nm BNNTs. Cation selectivity persisted for BNNT diameters of 12-nm and $C_H = 1$ M, for which the Debye length on the high-concentration side is smaller than the pore size. By contrast, 3-nm CNTs showed a rapid decline in selectivity with increasing C_H, which is typical of Donnan-type (charge-based) exclusion[24]. This is believed to result from the screening of the charged groups at the CNT tips as salt concentration increases. Thus, despite their identical crystallographic structure and diameter, the 3-nm BNNTs and CNTs showed very different ion selectivity because of their different surface-charge densities and the distribution thereof[25].

Intriguingly, measurements of ion transport in these BNNTs revealed atypical absolute rates of cation diffusion. As shown in Fig. 3a and Extended Data Fig. 1, the experiments demonstrated strikingly enhanced diffusion rates of K^+, Na^+ and Li^+ over Fickian diffusion in these BNNT pores. For Li^+, the per-pore fluxes were 21-fold and 31-fold higher than those expected for bulk diffusion in the 3-nm and 12-nm BNNTs, respectively. By comparison, the previously reported cation flux for a single 80-nm BNNT under the same KCl concentration gradient revealed an enhancement of 1.6-fold[10]. As discussed in more detail later, the order-of-magnitude larger enhancement in cation-diffusion rates for the present BNNTs is attributed to their smaller diameter, which increases the importance of surface transport relative to bulk diffusion. The enhanced cation mobility in BNNTs is also notable compared with CNTs of the same size (3 nm), as well as previous 4-nm-deep

https://doi.org/10.1038/s41565-026-02182-5

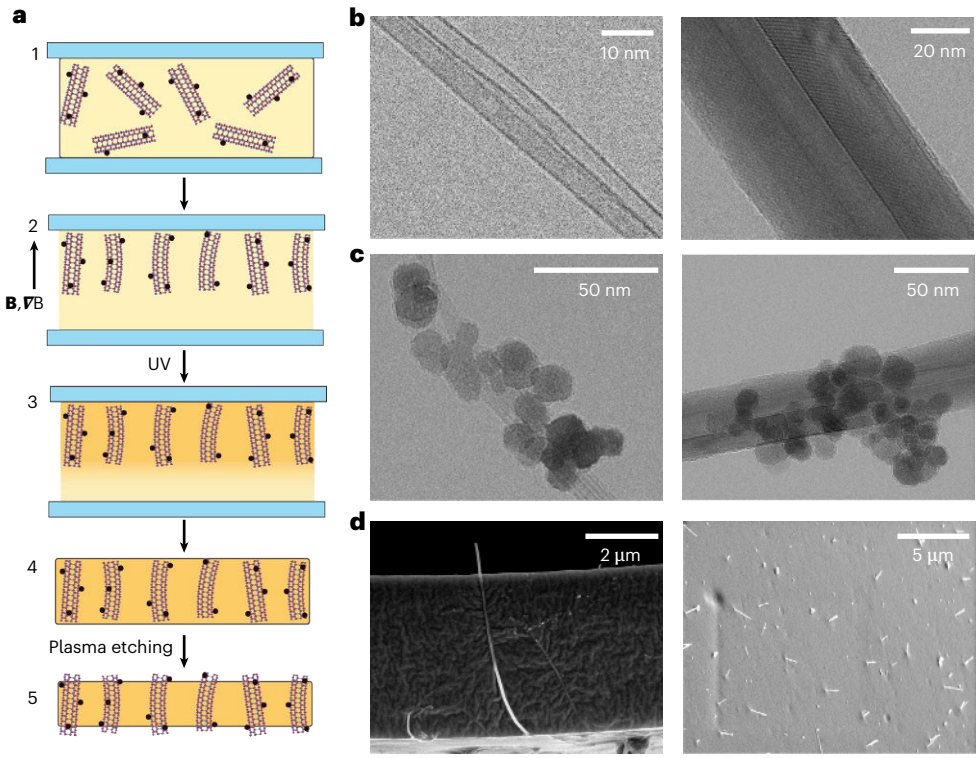


Fig. 1 | VA-BNNT and CNT membranes. a, Solution-based, field-assisted fabrication of VA-BNNT arrays: (1) magnetically functionalized BNNTs suspended in the liquid oligomer, (2) magnetic alignment and magnetophoretic deposition of nanotubes, (3) UV curing of urethane oligomer to the desired thickness, (4) extraction of urethane-embedded VA-nanotube array (total area ~20 cm^2) and (5) plasma etching to uncap nanotubes. **b**, Transmission electron microscopy image of 3-nm (left) and 12-nm (right) BNNTs. **c**, Fe_3O_4-nanoparticle decorated BNNTs with inner diameters of 3 nm (left) and 12 nm (right). **d**, SEM image showing aligned BNNT in the cross-section of the urethane matrix (left) and BNNT tips protruding from the top surface of the membrane (right).

2D silica nanochannels[23], both of which showed no enhancement in diffusive cation flux over bulk rates ($J^+/J^+_{\text{Fickian}} < 1$). Note that these calculations of cation-transport enhancement in the BNNT arrays are inherently conservative because they come from the measured current and assume that only cations are diffused through the nanotubes, that is, $I = q(J^+ - J^-) \approx qJ^+$. As the BNNTs showed transference numbers close to but not exactly 1 (Fig. 2c,d), the actual transport rate of cations is probably slightly greater than shown in Fig. 3a.

To interpret the enhanced absolute rate of cation diffusion, we first considered a continuum explanation based on the osmotic pressure-driven flux of concentrated cations in one-dimensional (1D) nanotubes. To screen the measured wall surface-charge density of $\Sigma = -170$ mC m^{-2} in the 12-nm BNNT, the average cation concentration in the electrical double layer ($\lambda_D \approx 10$ nm) would need to be $\Sigma/\lambda_D \approx 0.2$ M, two orders of magnitude higher than the bulk concentration on the low-molarity side ($C_L = 1$ mM). Then, an osmotic-pressure gradient can drive the concentrated cations in the double layer, resulting in a diffusio-osmotic current[10],

$$I_{\text{OSM, total}} = N\frac{2\pi R_p}{L_p}|\Sigma|\frac{k_B T}{\eta\lambda_B} ln\left(\frac{C_H}{C_L}\right), \quad (3)$$

where N is the pore number, R_p is the pore radius, L_p is the pore length, η is the viscosity and λ_B is the Bjerrum length.

We have compared this prediction with the measured osmotic currents in the present 3-nm and 12-nm BNNT arrays, as well as previous single BNNTs of larger diameters[10]. The per-pore osmotic currents for KCl in all of the BNNTs collapse onto a single line when plotted against $(R_p/L_p)\Sigma \log(C_H/C_L)$ (Fig. 3b). The agreement shown in Fig. 3b between the data and theory over three orders of magnitude in osmotic current, with no adjustable parameters, provides strong evidence that diffusio-osmosis is the primary mechanism for enhanced, cation-selective transport in the charged BNNTs. Moreover, the collapse of the per-pore current for both the present BNNT arrays and the previously studied individual BNNT shows that the total osmotic current scales linearly with pore number up the maximum-studied pore density of 6.9×10^6 pores cm^{-2}. This is probably because the average spacing between the nanotubes at this pore density is on the order of 4 µm, which remains much larger than the diameter of the BNNTs and is similar to the membrane thickness. By contrast, in arrays of pores in an ultrathin, 2D silicon-nitride membrane, a subadditive ionic transport has been found[26]. Finally, the osmotic current can be seen to scale with R_p. As a result, the current or power density scales inversely with pore diameter, highlighting the advantage of ultranarrow nanotubes such as the 3-nm BNNTs used in this study. Overall, the enhanced absolute rates of cation diffusion in the BNNTs can be rationalized in a continuum sense (equation (3)) as arising from diffusio-osmosis of concentrated ions in the electrical double layer within the charged pores.

Anomalous lithium-ion transport

However, the data also revealed an anomalous relative transport of alkali-metal cations that cannot be explained by continuum diffusio-osmosis. Figure 3a shows that the apparent diffusion rates of K^+, Na^+ and Li^+ in BNNTs differed by up to 4.2-fold but in the opposite order to their known mobilities in bulk solution[27]. In bulk solution, Li^+ (a small ion with a strong hydration shell) has a lower diffusivity than Na^+ and especially K^+. However, in the narrow, charged BNNTs, the diffusive transport of cations was ordered as $J_{Li+} > J_{Na+} > J_{K+}$, in the opposite order to their hydrated ion mobility. Notably, the faster relative transport of Li^+ is not limited to concentration gradient-driven diffusion in the BNNTs but is also seen in the electric field-driven ionic conductance. As shown in Fig. 3c and Extended Data Fig. 2, the ionic

https://doi.org/10.1038/s41565-026-02182-5

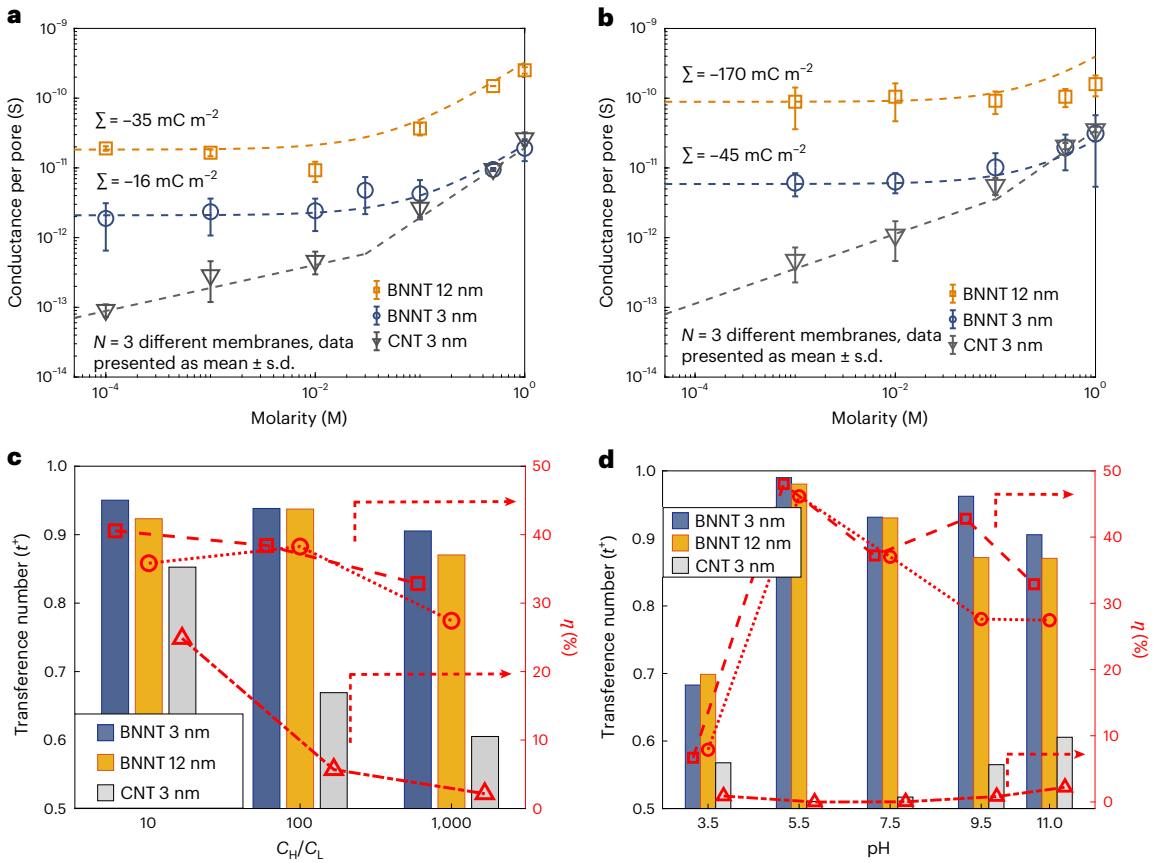


Fig. 2 | Surface-dominated conductance and cation-selective transport in BNNTs compared with CNTs. a, Single-pore conductance and fitted surface-charge density for BNNTs and CNTs in KCl solution at pH 7. **b**, KCl conductance and surface-charge density at pH 11. **c**, High K^+ cation selectivity and osmotic energy-conversion efficiency of BNNT membranes at pH 11, with transference numbers $t^+ \approx 1$ even for $C_H = 1$ M. **d**, Cation selectivity and energy-conversion efficiency for VA-BNNT and CNT membranes as a function of pH in a 1 mM:1 M KCl concentration gradient.

conductance of the BNNT arrays diverged substantially for KCl, NaCl and LiCl solutions at low molarities, with LiCl giving the highest conductance for $C_s < 100$ mM. By contrast, ionic conductances for 3-nm CNTs pores are nearly identical for the different salt solutions, with only a small difference (KCl having the highest conductance) that is consistent with the difference in hydrated size and bulk mobilities of Li^+, Na^+ and K^+ cations in solution. Furthermore, the ordering of cation transport rates in the BNNTs is also different from what has been previously reported for 2D BN nanochannels[12,13] and 2D graphene-oxide (GO) nanochannels[28]. The BNNTs showed both diffusive and electric field-driven (conductance) transport rates that were anomalously enhanced for Li^+ compared with that of Na^+ or especially K^+, in contrast to both CNTs and 2D nanofluidic channels.

The anomalous relative transport rates for different alkali-metal ions in the BNNTs are not only distinct from observations in previous experiments but also differ from what is predicted for diffusio-osmosis. The diffusio-osmotic model of equation (3) does not differentiate between different cations of the same charge, such as monovalent Li^+, Na^+ and K^+. While differences in anion-to-cation diffusivities can generate an electric field of $E_{diff} = \frac{k_B T}{q} \beta \nabla \log C$, where $\beta \equiv (D^+ - D^-)/(D^+ + D^-)$[29,30], the osmotic current produced by this self-generated field is estimated to be an order of magnitude smaller than what we measure (see the Methods for the calculations). In addition, anions are nearly completely excluded in these charged, small-diameter BNNTs ($t^+ \to 1$ in Fig. 2c,d), so $\beta \approx 1$ independent of the salt type, and we would not expect to see salt-specific differences in diffusive transport in BNNTs. We emphasize that the anomalous ordering of cation transport rates also extends to conductance experiments (Fig. 3c) in which the solution molarities are equal on both sides of the BNNTs and transport is driven by an external electric field rather than diffusion. This is additional evidence that the electrophoretic term associated with the difference in mobility of cations and anions does not fully explain the observed anomalous relative transport rates. For these multiple reasons, it does not appear plausible that the self-generated E_{diff} can explain the anomalous relative transport rates of different cations in the BNNTs. Furthermore, the ordering of ion transport rates observed in BNNTs is opposite to what has been reported for electrical conductance in angstrom-scale 2D BN channels, despite both systems having the same hexagonal BN walls and surface properties[12]. For all of these reasons, the ion-specific diffusion rates and conductances observed in BNNTs are quite unexpected.

Ab initio calculations

These results suggest that transport in BNNTs is strongly influenced by ion-specific interactions within the nanotube. To elucidate such interactions, we performed ab initio calculations of OH^- and each of the metal hydroxides on a 2D BN flake, as well as inside a periodic BNNT supercell with a 3-nm diameter and 1-nm tube length (Extended Data Figs. 3 and 4). As presented in Table 1, both calculations indicate that the dissociation energy of OH^- from the BN surface is substantially reduced when interacting with free alkali-metal cations. Moreover, the binding energy of LiOH is approximately half of that of KOH to the BN surface. The BNNT calculations further reveal that the presence of multiple metal hydroxides inside the nanotube additionally reduces their average binding energy. On the basis of these findings, we hypothesize that Li^+ can promote the release of OH^- from the inner walls of the BNNTs.

https://doi.org/10.1038/s41565-026-02182-5

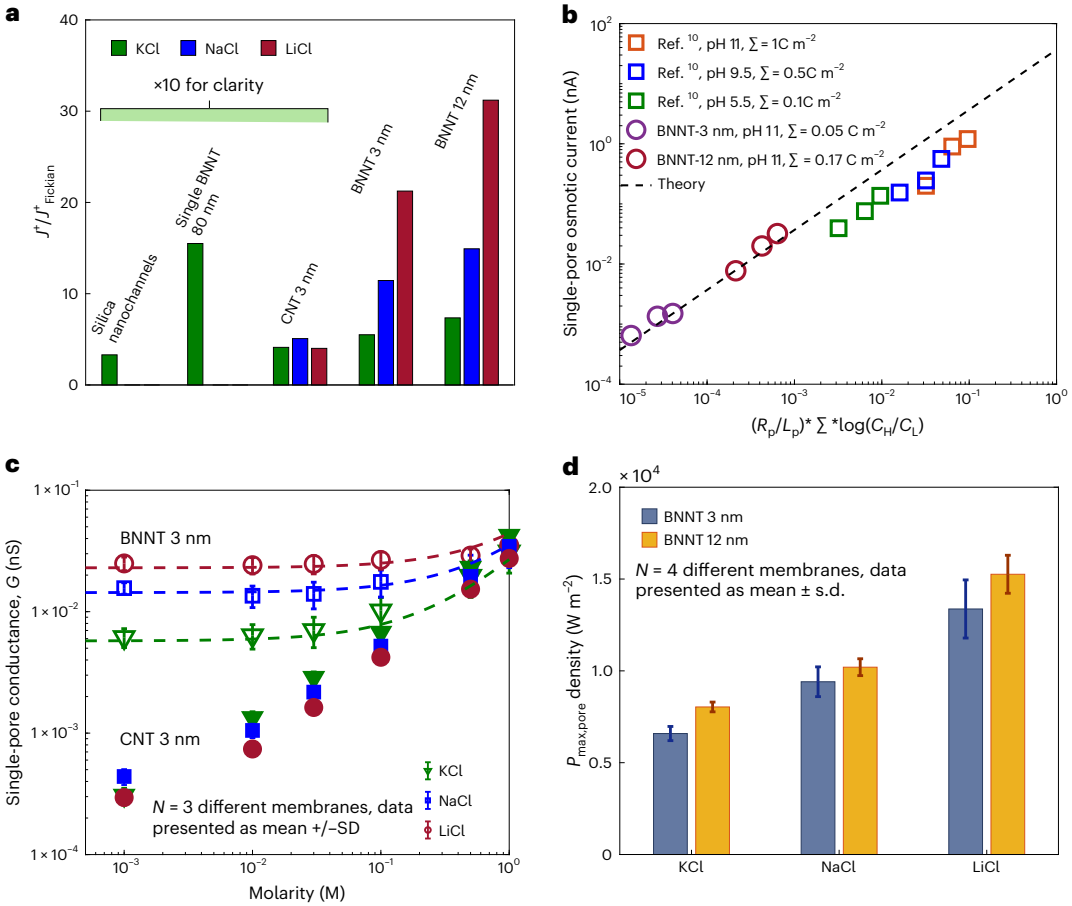


Fig. 3 | Enhanced, anomalous diffusion of different cations in BNNTs. **a**, Diffusion rates of different cations in various nanotubes compared with bulk diffusion expectations. Note that the relative transport rates in 4-nm silica nanochannels[23], 3-nm CNTs and the single 80-nm BNNT[10] are multiplied tenfold for clarity, that is, they are more than an order of magnitude lower than that in the 3- and 12-nm BNNTs. **b**, Scaling of per-pore current compared with diffusio-osmotic predictions of equation (3). The 3- and 12-nm BNNT arrays of the present work are compared with single BNNTs of different pore diameter, length and surface-charge density in KCl solutions of different pH and concentration gradients. **c**, Per-pore conductance for 3-nm BNNT and CNT arrays for various salts at pH 11. **d**, Per-pore power density for 1 mM:1 M concentration difference for different salts at pH 11.

Table 1 | Ab initio dissociation energies from BN surfaces in planar and cylindrical configurations (Extended Data Figs. 3 and 4)

Species	Binding energy on planar BN (eV)	Binding energy in 3-nm BNNT (eV)	Average binding energy of ten hydroxides in 3-nm BNNT (eV)
LiOH	−0.15	−0.7	−0.3
NaOH	−0.32	−1.1	−0.5
KOH	−0.35	−1.1	−0.6
OH	−0.52	−3.7	−3.8

Kramers' theory

Continuum analysis supports the hypothesis that ion-specific interactions between cations and charged OH^- groups on the interior of the BNNTs can drastically affect the ion transport. To qualitatively estimate these effects, we can model these local interactions with an additional potential, where the potential depth Q varies for different species, for example, Li^+ versus K^+. The fraction of cations trapped in the energy wells can be shown to be

$$f = \frac{1}{1 + \alpha_1 e^{-Q/k_B T}}. \quad (4)$$

Then, Kramers' theory[31,32] gives a reduced effective mobility for cations trapped in the wells,

$$\mu_B^+ = \mu^+ \alpha_2 e^{-Q/k_B T}, \quad (5)$$

where α_1 and α_2 are dimensionless constants that depend on the detailed profile of the energy barrier. An important implication of equation (5) is that small differences in the ion-surface interaction (that is, the potential well depth Q) can have an exponential impact on the effective mobility of various cations. Thus, different binding energies of the hydroxides and their varying likelihood of removal from the surface could substantially affect the transport of different species in the BNNTs.

MD simulations

Next, we performed atomistic molecular dynamics (MD) simulations to study the effect of the hypothesized OH^- release on the relative transport of the different ions in the BNNTs. Three different scenarios were considered: (1) the same number of explicit, fixed OH^- groups on the interior of the BNNT for all three solutions, (2) different numbers of explicit OH^- groups for the three solutions and (3) the same distributed wall charge of 30 e^- but differing numbers (ten for KCl, five for NaCl and zero for LiCl) of explicit OH^- groups on the interior. The last scenario is motivated by the observation that, by reducing the binding energy of the OH^- surface group, Li^+ may be in effect making some of the surface charge mobile,

https://doi.org/10.1038/s41565-026-02182-5

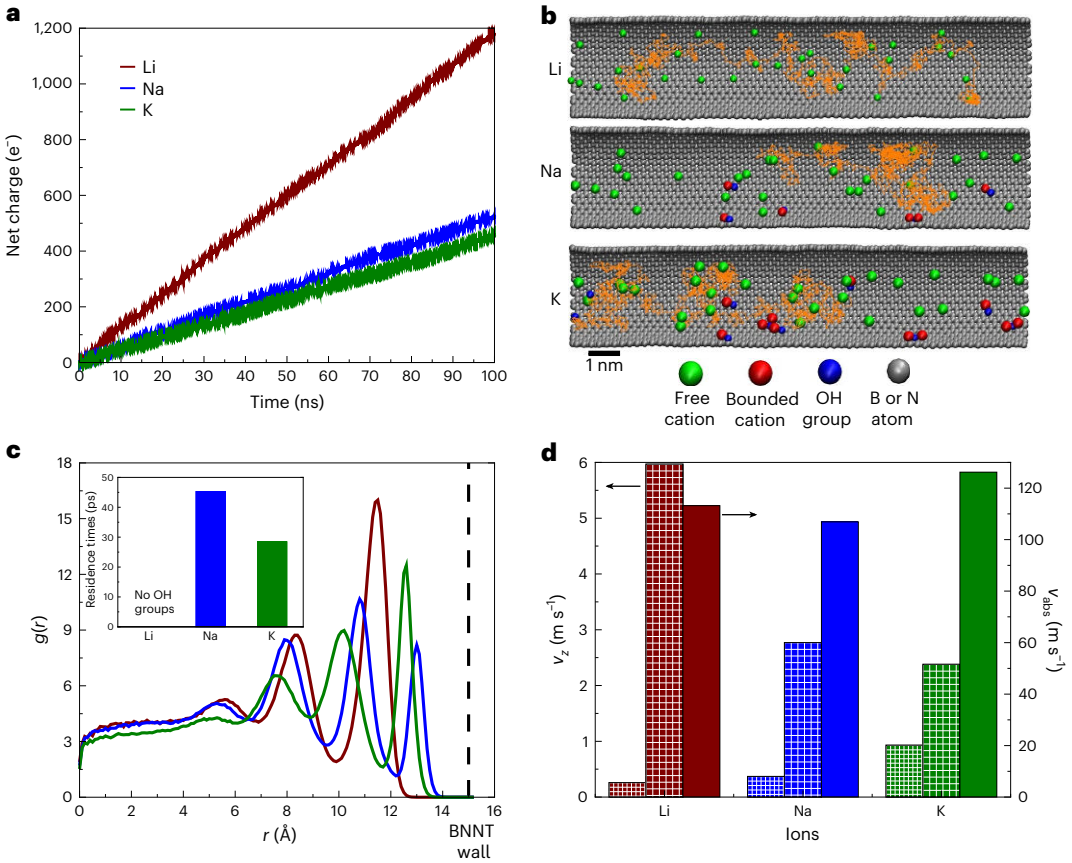


Fig. 4 | MD simulations of ion transport in differently charged BNNTs. a, Net charge of ions passed through (22,22) BNNT with uniformly distributed charge of $q = 30\ e^-$ and ten additional OH^- surface groups in the K^+ system, five additional OH^- groups in the Na^+ system and no additional interior OH^- groups in the Li^+ system. **b**, Trajectory of randomly selected free cation (green) in the tube during last 2.5 ns of simulation (100-ns long). **c**, Radial distribution of ions with respect to the centre of the BNNT. Inset: residence times of the ions bonded to interior OH^- groups. **d**, Average axial velocities of cations (patterned bars), as well as absolute velocities (solid bars). Bars with larger box patterns show axial velocities for BNNTs with 30 distributed charges and 0, 5 and 10 OH^- groups for Li, Na and K cases, respectively. Bars with smaller box patterns show axial velocities for BNNTs with no distributed charge and 40 discrete OH^- groups. Solid bars show absolute velocities for the cases with 30 distributed charges and varying OH^- groups.

that is, physisorbed rather than chemisorbed[20], which could be approximated by the distributed charge on the wall. Moreover, in real multiwalled BNNTs, a portion of the 'surface' charge could come from the outer BN walls and/or the matrix material[33] and would presumably remain even if OH^- is released from the inner BN surface. The interior of the nanotube would not be shielded from these outer charges because the BN walls are insulating. However, as polarization is likely to smear the electric fields produced by the outer charges, we have distributed a homogeneous charge of 30 e^- on a single-wall BNNT. An additional ten OH^- groups were placed on the inner wall in the KCl case, compared with five OH^- groups for NaCl and none for LiCl, as shown in Fig. 4b. Thus, the total charge was 40 e^-, 35 e^- and 30 e^- for KCl, NaCl and LiCl cases, respectively.

As shown in Extended Data Fig. 5, in the first scenario, when the whole charge (40 e^-, equivalent to a density of −45 mC m^{-2}; Fig. 2b) originates from OH^- groups attached to the interior surface of the tubes, we obtained currents that had the opposite ordering to the experiments. Likewise, as seen in Extended Data Fig. 6, when we simulated the second scenario with explicit OH^- groups corresponding to surface-charge densities of $\Sigma_{w,Li} = -310$ mC m^{-2}, $\Sigma_{w,Na} = -140$ mC m^{-2} and $\Sigma_{w,K} = -45$ mC m^{-2} (Fig. 3c), we also found $J_{Li+} < J_{Na+} < J_{K+}$. In both of these cases, despite the equal or higher surface-charge density that attracted counterions into the BNNT, the Li^+ cations were particularly trapped by the fixed OH^- groups.

Only when the experimentally observed surface charge is partially distributed on the BNNT, with reduced OH^- numbers inside the BNNT depending on the likelihood of release, did we obtain currents that matched the ordering observed in the experiments for the three salts. As shown in Fig. 4c, the radial distribution functions and residence times indicate that the Li^+ ions were no longer bound to the wall in the absence of interior OH^- groups. As a result, the Li^+ ions showed the fastest axial (z component) velocity, v_z (Fig. 4d), although the K^+ ions still had the fastest absolute velocities, v_{abs}. Thus, despite having the lowest total surface charge (30 e^- for LiCl versus 40 e^- for KCl), the BNNTs filled with LiCl solutions produced the highest current in our simulations (Fig. 4a). For the three alkali-metal ions simulated, the currents were ordered as $J_{Li+} > J_{Na+} > J_{K+}$, consistent with experiments (Fig. 3a,d). By contrast, as shown in Extended Data Figs. 5 and 6, the presence of fixed OH^- groups on the surface invariably reduced the axial mobility of Li^+ compared with other cations, thereby reducing its ionic current. These combined density functional theory (DFT) and MD simulation results support the hypothesis that the anomalous relative transport rates of different alkali-metal cations are due to the Li-promoted release of charged OH^- groups on the inner BN surface. This may effectively convert the OH^- from being chemisorbed to physisorbed, which has been shown in simulations to increase interfacial mobility and ionic conductivity[20]. We emphasize that our classical MD simulations and ab initio modelling with implicit water are our first approximation. Polarizable MD simulations or even full ab initio modelling with molecular water are desirable to validate the conclusions and quantify the surface reactions and OH^- dynamics in different solutions.

Discussion

While the proposed mechanism of enhanced transport due to Li-promoted OH^- release has only been tested in MD simulations of electric field-driven transport, it may have implications for diffusive transport as well. Specifically, while equation (3) for diffusio-osmotic current explicitly depends on surface-charge density (and not mobility), the charge density Σ_w could be considered an effective surface-charge density. Indeed, the standard practice is to calculate Σ_w from ionic conductance measurements using equation (1) or similar expressions[10,23]. However, the conductance measurements actually give the product of mobility and surface charge: $\mu\Sigma_w$. Thus, the very large surface-charge densities for BNNTs reported in this Article and by Siria et al. (up to 1 C m^{-2} in the case of the latter) may be a consequence of the enhanced ionic mobilities under certain circumstances. This would suggest that the surface-charge density Σ_w in equation (3) for diffusio-osmotic current should either be viewed as an effective charge density or potentially revised to account for differing effective ion mobilities. Furthermore, theoretical work by Bonthuis and Netz indicates that there is a difference between conductive surface charge density (which can be found by conductance measurements) and an electrokinetic surface charge density (which can be found from the streaming potential using the Grahame equation)[34]. This is primarily due to the enhanced condensation of ions close to the surface resulting from the low effective dielectric constant of interfacial water. For these reasons, it may be desirable to re-examine whether the experimental surface-charge density for electric field- and diffusive-driven transport in BNNTs is more properly viewed as an actual surface-charge density or an effective one potentially influenced by differing ion mobilities.

While considerable challenges remain in terms of scale-up and increasing areal power density, the fast, ion-selective transport in BNNTs could potentially enable membranes for applications such as lithium recovery or electricity generation by harvesting 'blue' energy from concentration gradients at natural estuaries or desalination plants[35–38]. As per-pore power density scales as Σ_w/R_p (see equation (2) and Fig. 3b), decreasing the pore size substantially increases the power density compared with previous, larger-diameter BNNTs. As shown in Fig. 3d, the 3- and 12-nm BNNT arrays show per-pore power densities exceeding 7,500 W m^{-2} for 1 mM:1 M KCl solutions and 15,300 W m^{-2} for LiCl at pH 11. This is a notable improvement over the 4,000 W m^{-2} found for the single 80-nm BNNT studied previously under similar conditions[10]. The osmotic power increased linearly with surface-charge density (which was varied by changing pH), as well as with the log of the concentration gradient across the membrane, as shown in Extended Data Fig. 1. As a result of their high cation selectivity, for a pH between 5.5 and 9.5, the BNNT arrays achieved osmotic-energy conversion efficiencies $\eta_{max} = \frac{(2t^+-1)^2}{2}$ (ref. 23) approaching the maximum of 50% for an individual ion-exchange membrane, as shown in Fig. 2c,d. Higher efficiencies are only possible for pairs of cation- and anion-selective membranes. The conversion efficiencies of the BNNTs were notably higher than the $\eta \lesssim 10\%$ of CNTs of the same diameter, the η = 8% of 4-nm-high 2D silica nanochannels[23] and the η = 17.6% of 5-nm-diameter nanopores in MoS_2 nanosheets[8].

For scale-up, the solution-based, field-assisted method for fabricating membranes with VA nanotubes is flexible with respect to the type of nanotube used and is potentially compatible with roll-to-roll processing. The present membranes demonstrate considerable increase in size and total current over previous work, with 1-cm^2 BNNT arrays generating an overall current that is 10^4-fold greater (10 μA versus 1 nA) than that of the single 80-nm BNNT of previous studies[10] (Extended Data Fig. 7 and Extended Data Table 1). As a proof of concept, we have powered a calculator, watch and LED using a stack of eight 1-cm^2 BNNT arrays in series (Extended Data Figs. 8 and 9 and Supplementary Videos 4–6). Further improvements in areal power density and the total power of the membrane could be achieved by decreasing nanotube diameter and increasing the pore density. It would be particularly helpful to increase the open-pore percentage, as it is currently estimated that less than 1% of the available BNNTs are serving as through pores.

Conclusion

These results show that ion transport in narrow BNNTs is enhanced with respect to bulk and highly selective for specific cations, particularly Li^+. The marked difference in both ionic diffusion and conductance between BNNTs and CNTs—which exhibit negligible osmotic power generation but substantial enhancement in water flow[3,15,39,40]—highlight the subtle but important differences in surface chemistry and charge that govern ion transport in otherwise dimensionally and crystallographically similar 1D nanotubes. The quasi-1D confinement of ions in BNNTs also appears to be fundamentally different from 2D confinement in BN nanochannels, as evidenced by the different ordering of ionic conductance for various alkali-metal ions between the two systems. Because of the surface-dominated diffusio-osmotic transport in charged, 1D BNNTs, the overall transport of cations is enhanced by more than an order of magnitude over bulk values. Moreover, species-specific interactions between cations and OH^- groups on the inner BN surface cause the relative transport rates of different alkali-metal ions to be anomalous, with Li^+ transported 4–7-fold faster than K^+, for instance. On the basis of ab initio calculations and MD simulations, we hypothesize that the preferentially enhanced transport of Li^+ may be due to OH^- groups being released from the hexagonal-boron-nitride surface and becoming mobile, effectively becoming physisorbed rather than chemisorbed. These unexpected phenomena, together with the scalable and flexible fabrication method that enables macroscopic membranes with different types of nanotubes, may offer opportunities to design nanotube membranes optimized for lithium recovery, energy conversion, desalination and other separation processes.

Online content

Any methods, additional references, Nature Portfolio reporting summaries, source data, extended data, supplementary information, acknowledgements, peer review information; details of author contributions and competing interests; and statements of data and code availability are available at https://doi.org/10.1038/s41565-026-02182-5.

References

1. Sint, K., Wang, B. & Král, P. Selective ion passage through functionalized graphene nanopores. *J. Am. Chem. Soc.* **130**, 16448–16449 (2008).
2. Rollings, R. C., Kuan, A. T. & Golovchenko, J. A. Ion selectivity of graphene nanopores. *Nat. Commun.* **7**, 1–7 (2016).
3. Tunuguntla, R. H. et al. Enhanced water permeability and tunable ion selectivity in subnanometer carbon nanotube porins. *Science* **357**, 792–796 (2017).
4. Gopinadhan, K. et al. Complete steric exclusion of ions and proton transport through confined monolayer water. *Science* **363**, 145–148 (2019).
5. Duan, C. & Majumdar, A. Anomalous ion transport in 2-nm hydrophilic nanochannels. *Nat. Nanotechnol.* **5**, 848–852 (2010).
6. Buchsbaum, S. F. et al. Fast permeation of small ions in carbon nanotubes. *Adv. Sci.* **8**, 2001802 (2021).
7. Tunuguntla, R. H., Allen, F. I., Kim, K., Belliveau, A. & Noy, A. Ultrafast proton transport in sub-1-nm diameter carbon nanotube porins. *Nat. Nanotechnol.* **11**, 639–644 (2016).
8. Feng, J. et al. Single-layer MoS2 nanopores as nanopower generators. *Nature* **536**, 197–200 (2016).
9. Graf, M. et al. Light-enhanced blue energy generation using MoS2 nanopores. *Joule* **3**, 1549–1564 (2019).
10. Siria, A. et al. Giant osmotic energy conversion measured in a single transmembrane boron nitride nanotube. *Nature* **494**, 455–458 (2013).

11. Li, Z. et al. Ion transport and ultra-efficient osmotic power generation in boron nitride nanotube porins. *Sci. Adv.* **10**, 8081 (2024).
12. Esfandiar, A. et al. Size effect in ion transport through angstrom-scale slits. *Science* **358**, 511–513 (2017).
13. Pendse, A. et al. Charged layered boron nitride-nanoflake membranes for efficient ion separation and water purification. *Small* **15**, 1904590 (2019).
14. Brown, M. S., Shan, J. W., Lin, C. & Zimmermann, F. M. Electrical polarizability of carbon nanotubes in liquid suspension. *Appl. Phys. Lett.* **90**, 203108 (2007).
15. Castellano, R. J. et al. Scalable electric-field-assisted fabrication of vertically aligned carbon nanotube membranes with flow enhancement. *Carbon* **157**, 208–216 (2020).
16. Cetindag, S. et al. Surface-charge effects on the electro-orientation of insulating boron-nitride nanotubes in aqueous suspension. *J. Colloid Interface Sci.* **505**, 1185–1192 (2017).
17. Erb, R. M., Libanori, R., Rothfuchs, N. & Studart, A. R. Composites reinforced in three dimensions by using low magnetic fields. *Science* **335**, 199–204 (2012).
18. Arcenegui, J. J., García-Sánchez, P., Morgan, H. & Ramos, A. Electro-orientation and electrorotation of metal nanowires. *Phys. Rev. E* **88**, 063018 (2013).
19. Grosjean, B. et al. Chemisorption of hydroxide on 2D materials from DFT calculations: graphene versus hexagonal boron nitride. *J. Phys. Chem. Lett.* **7**, 4695–4700 (2016).
20. Grosjean, B., Bocquet, M.-L. & Vuilleumier, R. Versatile electrification of two-dimensional nanomaterials in water. *Nat. Commun.* **10**, 1656 (2019).
21. Secchi, E., Niguès, A., Jubin, L., Siria, A. & Bocquet, L. Scaling behavior for ionic transport and its fluctuations in individual carbon nanotubes. *Phys. Rev. Lett.* **116**, 154501 (2016).
22. Cetindag, S. et al. Ion and hydrodynamic translucency in 1D van der Waals heterostructured boron-nitride single-walled carbon nanotubes. *ACS Nano* **18**, 355–363 (2023).
23. Kim, D. K., Duan, C., Chen, Y. F. & Majumdar, A. Power generation from concentration gradient by reverse electrodialysis in ion-selective nanochannels. *Microfluid. Nanofluidics* **9**, 1215–1224 (2010).
24. Fornasiero, F. et al. Ion exclusion by sub-2-nm carbon nanotube pores. *Proc. Natl Acad. Sci. USA* **105**, 17250–17255 (2008).
25. Pendse, A. et al. Intrinsic ion transport of highly charged sub-3-nm boron nitride nanotubes. *Mater. Today* **60**, 79–90 (2022).
26. Gadaleta, A. et al. Sub-additive ionic transport across arrays of solid-state nanopores. *Phys. Fluids* **26**, 012005 (2014).
27. Sahu, S., Ventra, M. D. & Zwolak, M. Dehydration as a universal mechanism for ion selectivity in graphene and other atomically thin pores. *Nano Lett.* **17**, 4719–4724 (2017).
28. Abraham, J. et al. Tunable sieving of ions using graphene oxide membranes. *Nat. Nanotechnol.* **12**, 546–550 (2017).
29. Anderson, J. L. Colloid transport by interfacial forces. *Annu. Rev. Fluid Mech.* **21**, 61–99 (1989).
30. Lee, C. et al. Osmotic flow through fully permeable nanochannels. *Phys. Rev. Lett.* **112**, 244501 (2014).
31. Kramers, H. A. Brownian motion in a field of force and the diffusion model of chemical reactions. *Physica* **7**, 284–304 (1940).
32. Mazo, R. M. *Brownian Motion: Fluctuations, Dynamics, and Applications* (Oxford Univ. Press, 2002).
33. Hong, C., Zhou, X., Ye, Y. & Li, W. Synthesis and characterization of UV-curable waterborne polyurethane–acrylate modified with hydroxyl-terminated polydimethylsiloxane: UV-cured film with excellent water resistance. *Prog. Org. Coat.* **156**, 106251 (2021).
34. Bonthuis, D. J. & Netz, R. R. Unraveling the combined effects of dielectric and viscosity profiles on surface capacitance, electro-osmotic mobility, and electric surface conductivity. *Langmuir* **28**, 16049–16059 (2012).
35. Siria, A., Bocquet, M.-L., Bocquet, L. New avenues for the large-scale harvesting of blue energy. *Nat. Rev. Chem.* https://doi.org/10.1038/s41570-017-0091 (2017).
36. Zhang, Z., Wen, L. & Jiang, L. Nanofluidics for osmotic energy conversion. *Nat. Rev. Mater.* **6**, 622–639 (2021).
37. Vermaas, D. A. et al. High efficiency in energy generation from salinity gradients with reverse electrodialysis. *ACS Sustain. Chem. Eng.* **1**, 1295–1302 (2013).
38. Pendse, A. et al. Highly efficient osmotic energy harvesting in charged boron-nitride-nanopore membranes. *Adv. Funct. Mater.* **31**, 2009586 (2021).
39. Holt, J. K. et al. Fast mass transport through sub-2-nanometer carbon nanotubes. *Science* **312**, 1034–1037 (2006).
40. Yang, D.-C. et al. Fast water transport through subnanometer diameter vertically aligned carbon nanotube membranes. *Nano Lett.* **23**, 4956–4964 (2023).

Publisher's note Springer Nature remains neutral with regard to jurisdictional claims in published maps and institutional affiliations.

Springer Nature or its licensor (e.g. a society or other partner) holds exclusive rights to this article under a publishing agreement with the author(s) or other rightsholder(s); author self-archiving of the accepted manuscript version of this article is solely governed by the terms of such publishing agreement and applicable law.

© The Author(s), under exclusive licence to Springer Nature Limited 2026

[1]Department of Mechanical and Aerospace Engineering, Rutgers University, Piscataway, NJ, USA. [2]Department of Chemical Engineering, University of Illinois at Chicago, Chicago, IL, USA. [3]Department of Chemistry, University of Illinois at Chicago, Chicago, IL, USA. [4]Materials Science Division, Argonne National Laboratory, Lemont, IL, USA. [5]Chasm Advanced Materials, Applications Development Center, Canton, MA, USA. [6]Department of Physics, University of California, Santa Barbara, Santa Barbara, CA, USA. [7]Department of Mathematics, Rutgers University, Piscataway, NJ, USA.
✉e-mail: pkral@uic.edu; sikim@uic.edu; jshan@soe.rutgers.edu

Methods

Fabrication of aligned BNNT membranes

To create arrays of VA-BNNTs embedded in a polymer matrix, functionalized nanotubes were dispersed in a UV-curable acrylated polyurethane oligomer, SU-710 (Soltech). A photoinitiator (Darocur 1173, BASF) was mixed with the liquid oligomer at a 5% vol. concentration. The mixture of photoinitiator and liquid oligomer was bath sonicated at 50 °C for 30 min and mixed with a vortex mixer for another 10 min before the introduction of nanotubes. Magnetically functionalized nanotubes were mixed in the oligomer mixture at a concentration of 1 mg ml^{-1} and bath sonicated at 50 °C for 30 min. The dispersed nanotube–liquid oligomer mixture was then placed in a fluidic setup consisting of two ITO-quartz slides with high transmission of UV light (OPCO Laboratory), separated by a 200-µm-thick double-sided tape spacer.

A 285-nm UV lamp illuminated the urethane oligomer through the UV-transparent ITO slides for a certain duration, typically a few seconds. The thickness of the cured matrix was varied by changing the duration of UV exposure. An initial calibration of thickness versus UV exposure duration was performed to enable curing of the target thickness of the membranes. Before curing of the liquid oligomer, nanotubes were aligned and deposited vertically in the fluidic setup with a magnetic field, as detailed in the Supplementary Discussion. Scanning electron microscopy (SEM) images of the VA-BNNTs protruding from the polymer surface are shown in Fig. 1d. The uncured, excess liquid oligomer on top of the cured film was then washed away by spraying acetone and deionized water. After the ~20-cm^2 BNNT arrays were fabricated, they were cut into smaller ~1-cm^2 sections and mounted on 200-µm-thick polymer supports for plasma etching and testing.

BNNT-array etching and thickness measurement. To eliminate the excess polymer and uncap the deposited BNNTs, a plasma-etching protocol was introduced. For etching, 1:1 (percentage mass flow rate) SF_6–O_2 gas was used in a plasma-etching system (March Instruments, PX250). Among these gases, SF_6 etches BN[41,42], while O_2 targets the excess polymer matrix. To check the effect of SF_6 on the hexagonal BN, exfoliated h-BN platelets were etched and examined under SEM. To reduce sample heating and defect generation in the cured polymer matrix, etching was done in multiple 1-min cycles at a plasma power of 100 W for each side until the target open-pore number was reached. After each cycle, measurements were made of the ion conductance and osmotic-power generation of the membranes to check for any possible defects. Typically, membranes with a starting thickness of 6.0-µm thickness were etched down to 5.0 µm after six or seven rounds of plasma etching on each side. Membrane thicknesses were measured using a thin-film measurement system using spectral reflectance (Filmetric F20-EXR) with a wavelength range of 400–1,700 nm. Before thickness measurement, light-exposure conditions were calibrated for SiO_2 on Si wafers with known thickness.

Ab initio calculations

We used first-principle methods to calculate the binding energies of LiOH, NaOH and KOH molecules to the passivated BN surface and compared them with the binding energies of the chemisorbed OH^- ions.

For 2D BN flakes, the calculations were done in implicit solvent (water) using the Conductor-like Polarizable Continuum Model (CPCM) method. All systems were calculated using the MP2/6 -311G** method and basis set using Gaussian 16 (ref. 43). We obtained the binding energies by subtracting the energies of attached and detached molecules as shown in Extended Data Fig. 3. In particular, the binding energies for the metal–OH and OH-to-BN surface (X + BN → X–BN) is defined as the enthalpy change for the reaction:

$$\Delta H_{\mathrm{bond}} = \Delta H_{X-\mathrm{BN}} - (\Delta H_X + \Delta H_{\mathrm{BN}}), \quad (6)$$

where X is OH, LiOH, NaOH or KOH.

For calculations of binding within a BNNT, a periodic BNNT supercell of 3 nm diameter and 1 nm of unit tube length was generated with 176 atoms of B and 176 atoms of N, as shown in Extended Data Fig. 4. We used a projector augmented-wave method and a plane-wave basis set implemented in Vienna[44,45], with an implicit solvation model for water using VASPSol[46,47]. We conducted two separate studies to calculate the binding strength of the metal hydroxides: (1) when one hydroxide ion and one cation are present and (2) when ten OH ions and ten cations are present. Density functional theory calculations were used to optimize the designed BN surface using the Vienna Ab Initio Simulation Package[44,45]. The projector augmented-wave formalism described the valence electrons of Li, Na, K, B, N, O and H atoms using plane wave-based wave functions[48]. The structure optimization, involving the minimization of ground state energy, used the generalized gradient approximation of Perdew and Wang and the PW91 functional[49,50]. A kinetic cut-off energy of 500 eV was set to enhance calculation accuracy. The Brillouin zone of the simulation cell with 240 atoms was sampled with 1 × 1 × 1k meshes for ionic optimization. Ionic and electronic optimizations were alternately performed until the forces on each ion reached less than ±10 meV $Å^{-1}$.

MD simulations

MD simulations were done with NAMD[51] using a CHARMM force field[52–57] and TIP3P water[58]. Langevin dynamics were used with a damping constant of $\gamma = 0.001$ ps^{-1}. Boron and nitrogen atoms within 2.5 Å from the ends of the tube were held fixed, whereas all other atoms were allowed to move freely. The time step was set to 2 fs. NVT ensemble was used at a temperature of $T = 298$ K. Particle mesh Ewald summation (PME) was used to describe long-ranged Coulombic interactions in the presence of periodic boundary conditions[59].

The simulated (22,22) BNNTs (radius of $r_0 \approx 1.5$ nm) were 15 nm long. Systems without reservoirs were placed in a box of a size of 11.7 nm × 11.7 nm × 15.2 nm. Systems with reservoirs had a box size of 11.7 nm × 11.7 nm × 55.1 nm, where there were two reservoirs, each 20 nm deep.

All simulations were initially minimized for 5,000 steps and then warmed for 2,000 steps at 1 K per five steps. During the production runs, an electric field of $E = 0.05$ MV cm^{-1} was applied to induce a current in each simulation. In the simulations of explicit OH^- groups, 40 OH^- groups and 40 cations were randomly placed inside the tube. The simulation atoms that were further than 5 Å away from the OH^- groups had a uniform charge to ensure charge neutrality in the system.

Data availability

The data supporting the findings of this study are available in this Article and its Supplementary Information.

References

41. Fröch, J. E., Hwang, Y., Kim, S., Aharonovich, I. & Toth, M. Photonic nanostructures from hexagonal boron nitride. *Adv. Opt. Mater.* **7**, 1801344 (2019).
42. Grenadier, S., Li, J., Lin, J. & Jiang, H. Dry etching techniques for active devices based on hexagonal boron nitride epilayers. *J. Vac. Sci. Technol. A* **31**, 061517 (2013).
43. Frisch, M. J. et al. Gaussian 16, Revision C.01 (Gaussian Inc., 2016).
44. Kresse, G. & Hafner, J. Ab initio molecular dynamics for liquid metals. *Phys. Rev. B* **47**, 558 (1993).
45. Kresse, G. & Hafner, J. Ab initio molecular-dynamics simulation of the liquid-metal–amorphous-semiconductor transition in germanium. *Phys. Rev. B* **49**, 14251 (1994).
46. Mathew, K., Sundararaman, R., Letchworth-Weaver, K., Arias, T. & Hennig, R. G. Implicit solvation model for density-functional study of nanocrystal surfaces and reaction pathways. *J. Chem. Phys.* **140**, 084106 (2014).

47. Mathew, K., Kolluru, V., Mula, S., Steinmann, S. N. & Hennig, R. G. Implicit self-consistent electrolyte model in plane-wave density-functional theory. *J. Chem. Phys.* **151**, 234101 (2019).
48. Blöchl, P. E. Projector augmented-wave method. *Phys. Rev. B* **50**, 17953 (1994).
49. Perdew, J. P., Burke, K. & Ernzerhof, M. Generalized gradient approximation made simple. *Phys. Rev. Lett.* **77**, 3865 (1996).
50. Burke, K., Perdew, J. P. & Wang, Y. in *Electronic Density Functional Theory: Recent Progress and New Directions* 81–111 (Springer, 1998).
51. Phillips, J. C. et al. Scalable molecular dynamics with NAMD. *J. Comput. Chem.* **26**, 1781–1802 (2005).
52. Crowley, M. F., Williamson, M. J. & Walker, R. C. Chamber: comprehensive support for CHARMM force fields within the AMBER software. *Int. J. Quantum Chem.* **109**, 3767–3772 (2009).
53. Vanommeslaeghe, K. & MacKerell Jr, A. D. Automation of the CHARMM general force field (CGenFF) I: bond perception and atom typing. *J. Chem. Inf. Model.* **52**, 3144–3154 (2012).
54. Vanommeslaeghe, K., Raman, E. & MacKerell Jr, A. D. Automation of the CHARMM general force field (CGenFF) II: assignment of bonded parameters and partial atomic charges. *J. Chem. Inf. Model.* **52**, 3155–3168 (2012).
55. Yu, W., He, X., Vanommeslaeghe, K. & MacKerell Jr, A. D. Extension of the CHARMM general force field to sulfonyl-containing compounds and its utility in biomolecular simulations. *J. Comput. Chem.* **33**, 2451–2468 (2012).
56. Vanommeslaeghe, K. et al. CHARMM general force field: a force field for drug-like molecules compatible with the CHARMM all-atom additive biological force fields. *J. Comput. Chem.* **31**, 671–690 (2010).
57. Best, R. B. et al. Optimization of the additive CHARMM all-atom protein force field targeting improved sampling of the backbone ϕ, ψ and side-chain χ_1 and χ_2 dihedral angles. *J. Chem. Theory Comput.* **8**, 3257–3273 (2012).
58. Jorgensen, W. L., Chandrasekhar, J., Madura, J. D., Impey, R. W. & Klein, M. L. Comparison of simple potential functions for simulating liquid water. *J. Chem. Phys.* **79**, 926–935 (1983).
59. Darden, T., York, D. & Pedersen, L. Particle mesh Ewald: An $N \cdot \log(N)$ method for Ewald sums in large systems. *J. Chem. Phys.* **98**, 10089–10092 (1993).
60. Cao, L. et al. Towards understanding the nanofluidic reverse electrodialysis system: well-matched charge selectivity and ionic composition. *Energy Environ. Sci.* **4**, 2259–2266 (2011).
61. Zhang, Z. et al. Engineered asymmetric heterogeneous membrane: a concentration-gradient-driven energy harvesting device. *J. Am. Chem. Soc.* **137**, 14765–14772 (2015).
62. Xin, W. et al. High-performance silk-based hybrid membranes employed for osmotic energy conversion. *Nat. Commun.* **10**, 3876 (2019).
63. Zhu, X. et al. Unique ion rectification in hypersaline environment: a high-performance and sustainable power generator system. *Sci. Adv.* **4**, 1665 (2018).
64. Gao, J. et al. High-performance ionic diode membrane for salinity gradient power generation. *J. Am. Chem. Soc.* **136**, 12265–12272 (2014).
65. Cheng, H. et al. Electrokinetic energy conversion in self-assembled 2D nanofluidic channels with Janus nanobuilding blocks. *Adv. Mater.* **29**, 1700177 (2017).
66. Hwang, J., Kataoka, S., Endo, A. & Daiguji, H. Enhanced energy harvesting by concentration gradient-driven ion transport in SBA-15 mesoporous silica thin films. *Lab Chip* **16**, 3824–3832 (2016).
67. Ma, T., Balanzat, E., Janot, J. M. & Balme, S. Nanopore functionalized by highly charged hydrogels for osmotic energy harvesting. *ACS Appl. Mater. Interfaces* **11**, 12578–12585 (2019).
68. Balme, S., Ma, T., Balanzat, E. & Janot, J. M. Large osmotic energy harvesting from functionalized conical nanopore suitable for membrane applications. *J. Membr. Sci.* **544**, 18–24 (2017).

Acknowledgements

This work was supported by NSF-CMMI/GOALI grant nos. 1762913 (to J.W.S. and R.F.P.) and 1762905 (to S.K.). We thank the Rutgers CryoEM & Nanoimaging Facility for transmission electron microscopy (TEM) imaging and Namrata Desai at the University of Illinois Chicago for scanning electron microscopy (SEM) imaging of the boron nitride nanotubes (BNNTs). We also thank BNNT LLC and Naieel Technology for providing BNNTs and Soltech Ltd. for providing oligomers used in this work.

Author contributions

J.W.S., S.K., R.F.P. and S.C. conceptualized the project. S.C. carried out the BNNT-membrane fabrication and characterization, ion-transport experiments and data analysis, with assistance from M.H., A.P. and J.Y. R.J.C. performed CNT-array fabrication and characterization. K.W. characterized the BNNTs and CNTs. R.J., S.C.S. and N.K.D. performed ab initio calculations of binding energies of hydroxides to BN surfaces. P.R. and V.K. carried out molecular-dynamics simulations with input from P.K. and A.T.N. P.K. proposed the presented explanation of anomalous currents. L.L. provided theoretical analysis of the effect of attractive potentials on diffusion near walls. J.W.S. and S.C. analysed data and wrote the manuscript, with input from all authors.

Competing interests

S.C., S.K., R.F.P., A.P. and J.W.S. are inventors on US patent application PCT/US2018/042157. All other authors declare no competing interests.

Additional information

Extended data is available for this paper at https://doi.org/10.1038/s41565-026-02182-5.

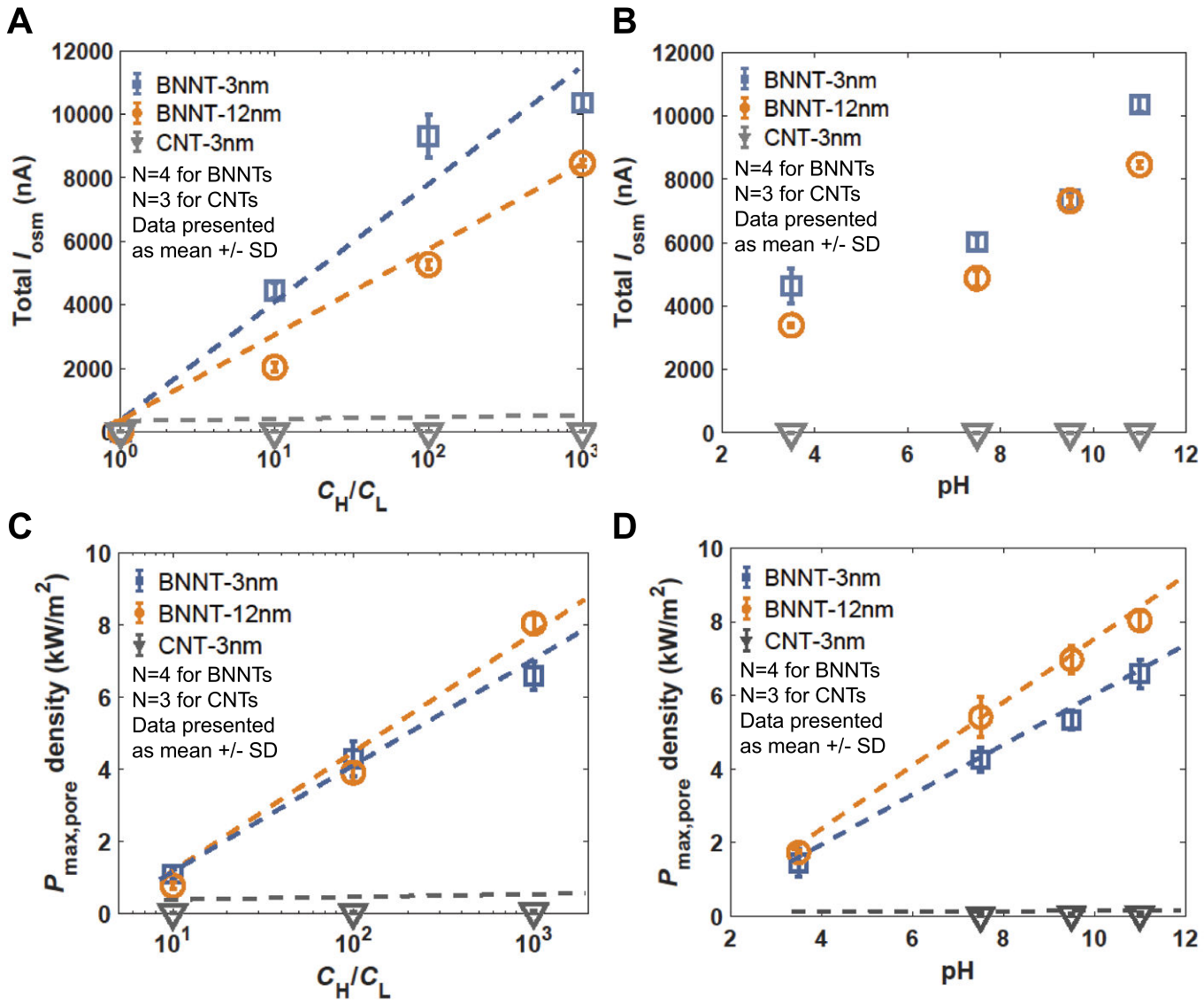
Supplementary information The online version contains supplementary material available at https://doi.org/10.1038/s41565-026-02182-5.

Correspondence and requests for materials should be addressed to Petr Kral, Sangil Kim or Jerry W. Shan.

Peer review information *Nature Nanotechnology* thanks the anonymous reviewer(s) for their contribution to the peer review of this work.

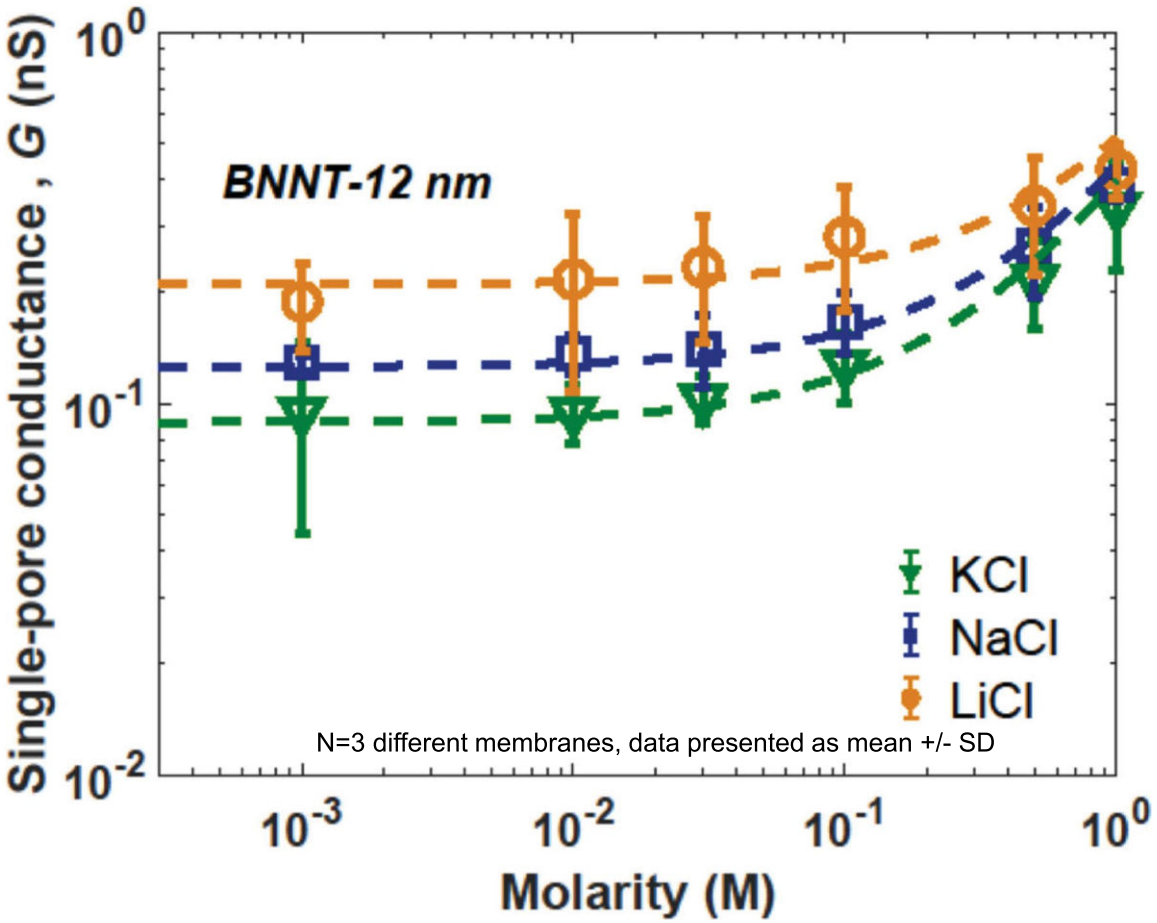
Reprints and permissions information is available at www.nature.com/reprints.

https://doi.org/10.1038/s41565-026-02182-5



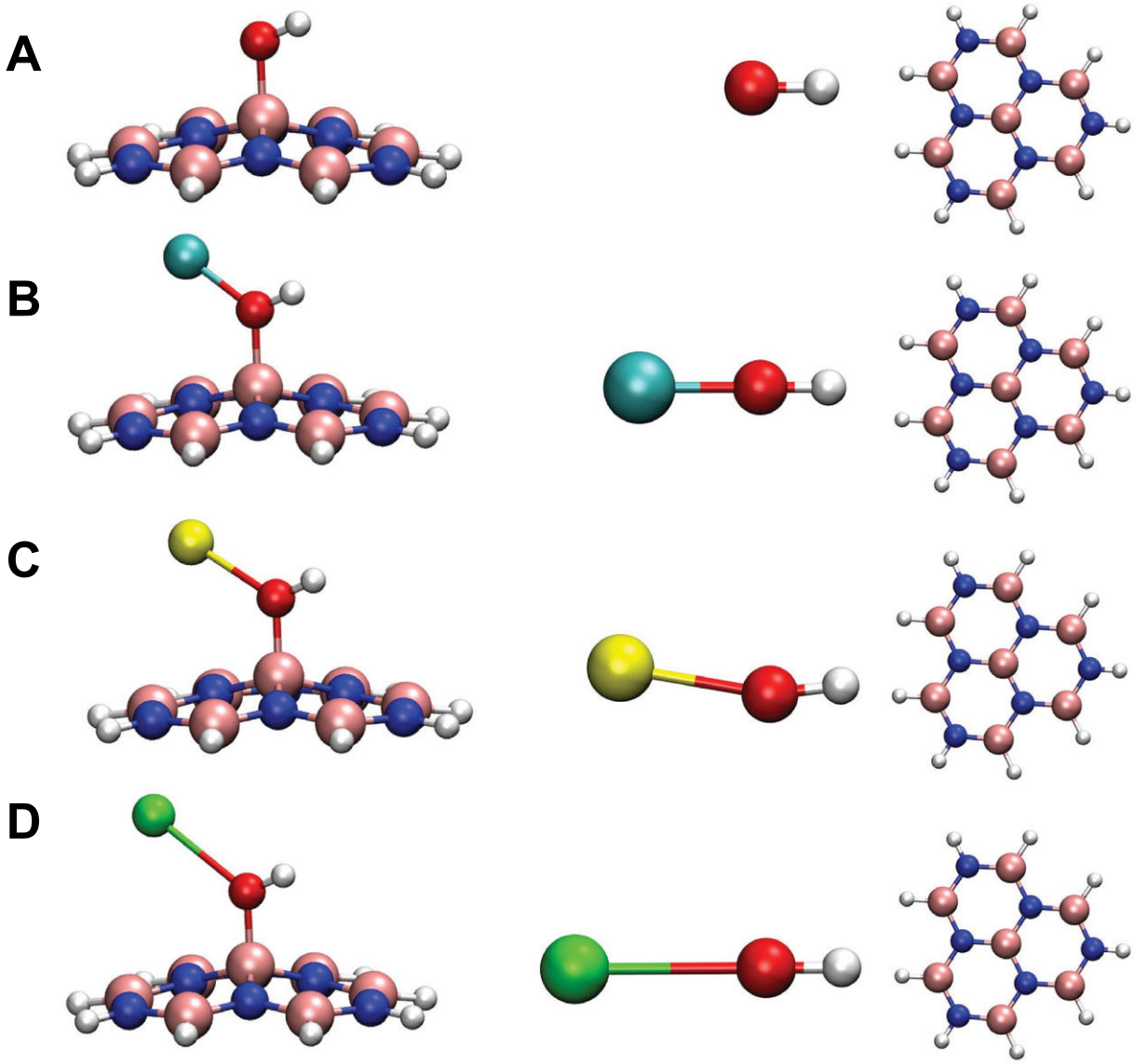
Extended Data Fig. 1 | Measured total osmotic currents and power densities for BNNT membranes in solutions of different pH and KCl concentration ratios. Measured osmotic currents and power densities for varying KCl concentration ratios and pH. (**a**) Total osmotic currents for C_H/C_L=1000:1 mM, 100:1 mM, and 10:1 mM at pH=11. (**b**) Total osmotic current at various pH for C_H/C_L=1000:1 mM. (**c**) Osmotic power densities for C_H/C_L=1000:1 mM, 100:1 mM, and 10:1 mM at pH=11. (**d**) Osmotic power densities at various pH for C_H/C_L=1000:1 mM.

https://doi.org/10.1038/s41565-026-02182-5



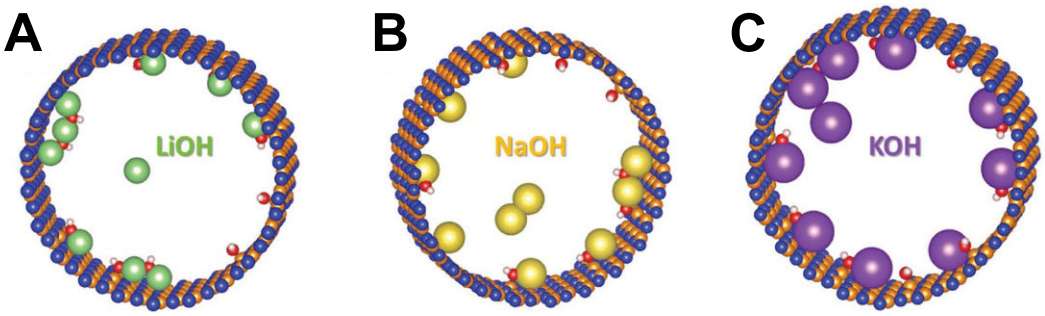
Extended Data Fig. 2 | Measured ion conductance of BNNT-12 nm membranes for different cations at pH=11. Ion conductance of BNNT-12 nm membranes for different cations at pH=11.

https://doi.org/10.1038/s41565-026-02182-5



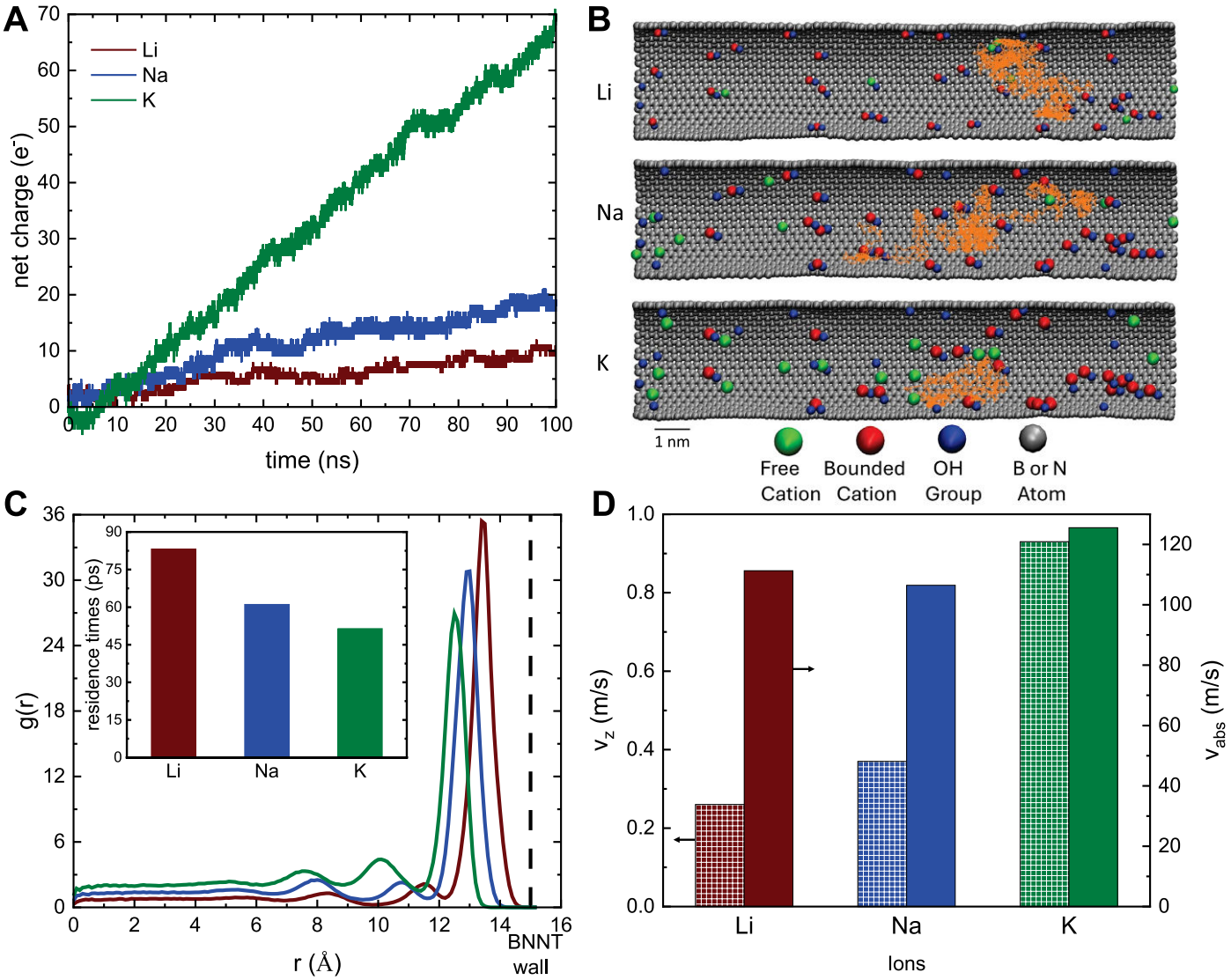
Extended Data Fig. 3 | Optimized structures for MP2/6-311G calculations on hydrogen-passivated BN flake.** Optimized structures for MP2/6-311G** calculations on hydrogen-passivated BN flake with: (**a**) OH^-, (**b**) LiOH, (**c**) NaOH, and (**d**) KOH.

https://doi.org/10.1038/s41565-026-02182-5



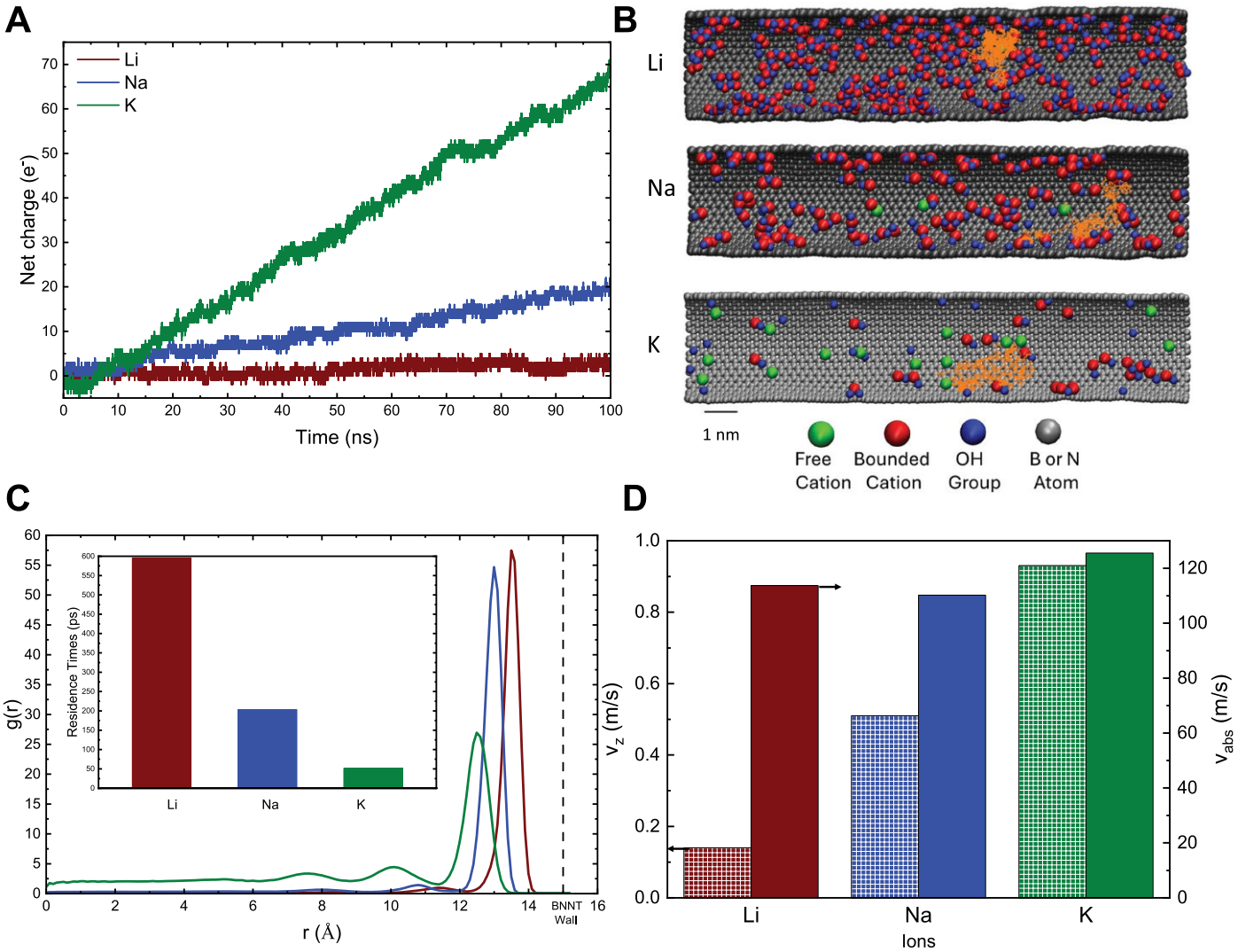
Extended Data Fig. 4 | Relaxed geometries of BNNT for ab initio calculations with 10 OH^- and 10 different cations. Relaxed geometries of BNNT along with 10 OH^- and 10 cations for ab initio calculations with: (**a**) Li^+, (**b**) Na^+, and (**c**) K^+.

https://doi.org/10.1038/s41565-026-02182-5



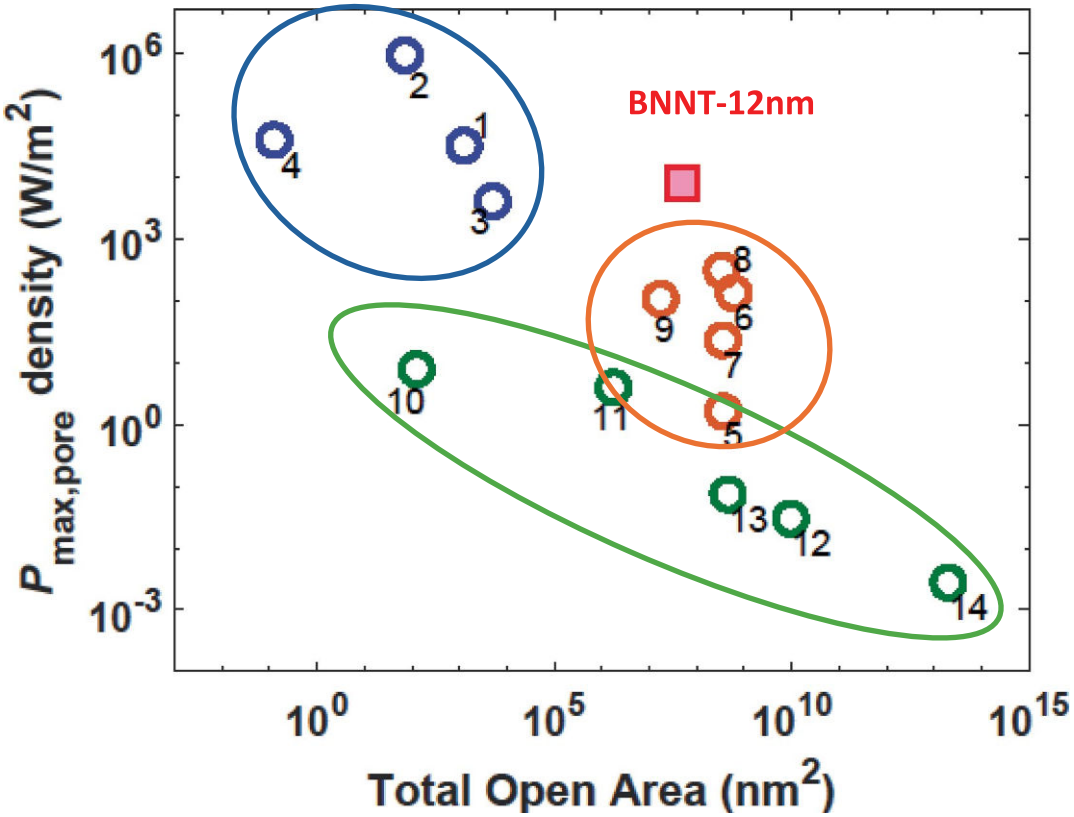
Extended Data Fig. 5 | MD simulations of ion transport in BNNT with 40 fixed OH^- groups on interior surface. MD simulations of ion transport in (22,22) BNNT with 40 OH^- groups on interior surface. (**a**) Net charge of ions passed through the tube. (**b**) Trajectories of randomly selected free cations (green) in tube during last 2.5 ns of simulation. (**c**) Radial distribution of ions with respect to the center of the BNNT. Inset: Residence times of the ions bonded to interior OH^- groups. (**d**) Average axial velocities of cations (patterned bars), as well as absolute velocities (solid bars).

https://doi.org/10.1038/s41565-026-02182-5



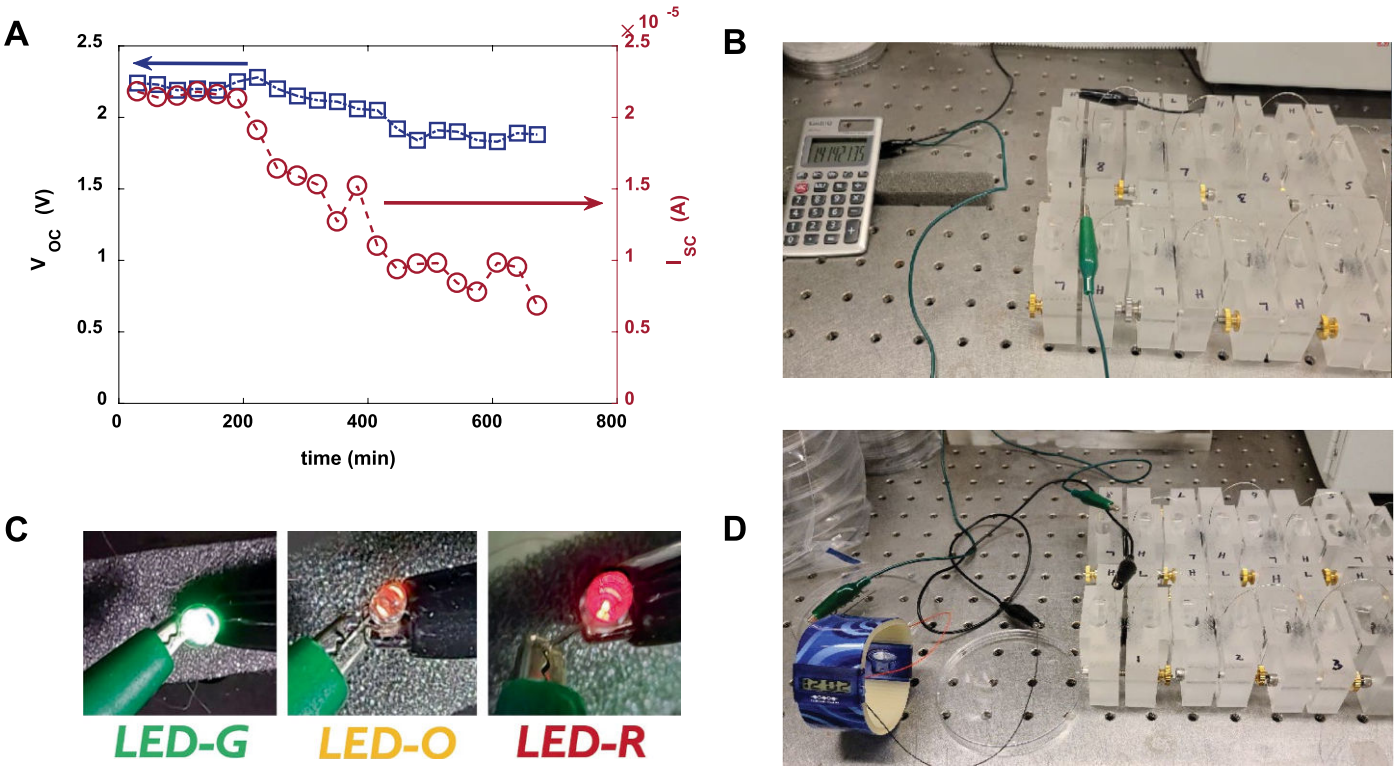
Extended Data Fig. 6 | MD simulations of ion transport in BNNTs with different fixed OH^- surface-charge densities for different salts. K^+ with 40 OH^-, Na^+ with 123 OH^-, and Li+ with 273 OH^-, corresponding to surface-charge densities of 45, 140, and 310 mC/m^2, respectively. (**a**) Net charge of ions passed through the tube. (**b**) Trajectories of randomly selected free cations (green) in tube during last 2.5 ns of simulation. (**c**) Radial distribution of ions with respect to the center of the BNNT. Inset: Residence times of the ions bonded to interior OH^- groups. (**d**) Average axial velocities of cations (patterned bars), as well as absolute velocities (solid bars).

https://doi.org/10.1038/s41565-026-02182-5



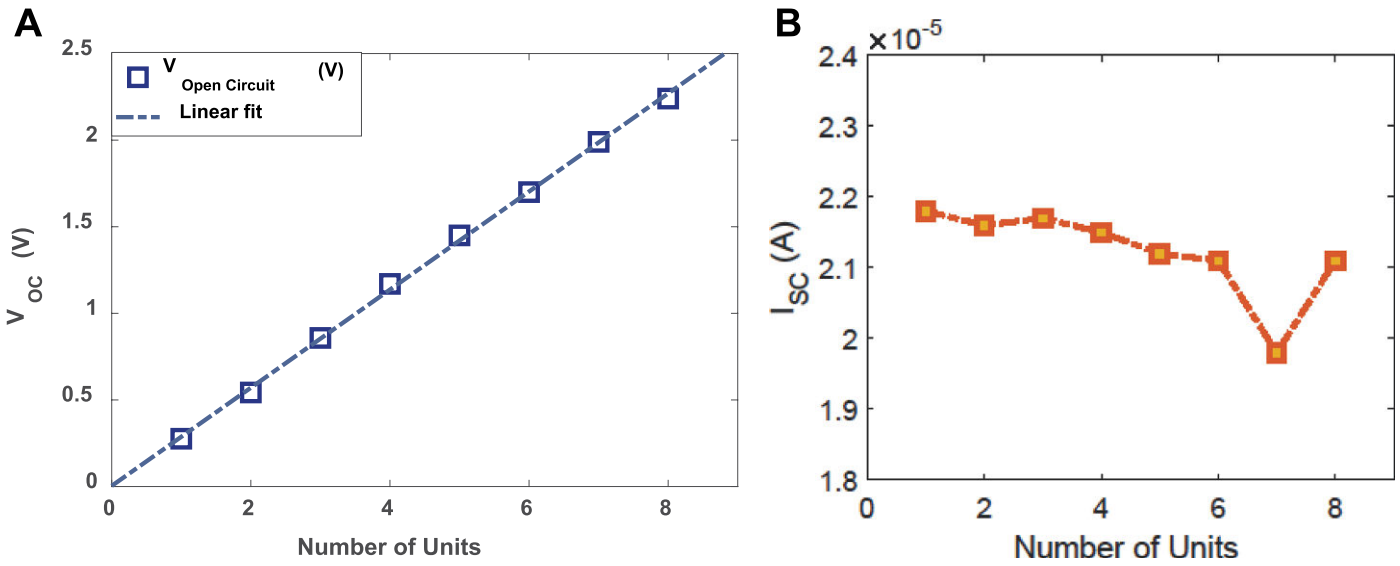
Extended Data Fig. 7 | Maximum power density and total pore area for the BNNT membranes compared to other osmotic power generation systems. The blue circle highlights single-pore nanosystems, while the orange circle shows ionic-diode type heterogenous systems. The green circle shows state-of-the-art macroscopic membranes. Data and references are given in Extended Data Table 1.

https://doi.org/10.1038/s41565-026-02182-5



Extended Data Fig. 8 | Demonstration of stack of 1 cm² BNNT membranes connected in series. (**a**) Open-circuit potential and short-circuit current over time for a stack of 8 BNNT membranes. Good stability is seen for 4 hours, followed by a decrease for longer durations. (**b**) Powering of a calculator, (**c**) LEDs of different colors, and (**d**) a watch with 8 BNNT membranes in series.

https://doi.org/10.1038/s41565-026-02182-5



Extended Data Fig. 9 | Electrical characteristics of BNNT-membranes osmotic generators connected in series. (**a**) Open-circuit potential for differing numbers of BNNT membranes in series. (**b**) Short-circuit current against the number of BNNT membranes in series.

https://doi.org/10.1038/s41565-026-02182-5

Extended Data Table 1 | Table comparing vertically aligned BNNT membranes with other single-pore and macroscopic systems

Label: Citation	Pore type	Pore diameter (nm)	Estimated power density (W/m^2)	Total open area (nm^2)	Maximum efficiency (%)
1: [60]	Polyamide NRED	40	31.8×10^3 (KCl, 1M-1mM)	1.26×10^3	29.3
2: [8]	Single-MoS_2	5	9.21×10^5 (KCl, 1M-1mM)	7.15×10^1	17.6
3: [10]	Single-BNNT	80	4.0×10^3 (KCl, 1M-1mM)	5.03×10^3	8.7
4: [3]	CNT-porin	0.4	39.3×10^3 (KCl, 0.1M-5mM)	1.26×10^{-1}	33.6
5: [61]	Porous block copolymer (BCP)	10	1.60 (KCl, 1M-1mM)	3.60×10^8	30.6
6: [62]	Silk nanofibril- AAO hybrid membrane	20	1.32×10^2 (KCl, 1mM-6μM)	6.06×10^8	12.9
7: [63]	PAEK-HS hybrid	8.5	22.8 (NaCl, 1M-10μM)	3.61×10^8	29.2
8: [64]	Carbon/Alumina hybrid	7	3.05×10^2 (KCl, 0.1M-6μM)	3.40×10^8	37.3
9: [65]	Kaolinite/Janus hybrid	0.68	1.60 (KCl, 1M-1mM)	1.73×10^7	47.1
10: [21]	Silica nanochannels	4	7.7 (KCl, 1M-0.1mM)	1.25×10^2	3.6
11: [66]	Mesaporous SBA15 - Silica	2	3.9 (KCl, 1M-1mM)	1.76×10^6	45.8
12: [67]	Charged hydrogel	156	3.0×10^{-2} (NaCl, 1M-1mM)	9.59×10^9	5.8
13: [68]	Chitosan/PAA conical nanopore	12	7.4×10^{-2} (NaCl, 1M-1mM)	4.59×10^8	N/A
14: [35]	Nafion based paper RED	N/A	2.8×10^{-3} (KCl, 0.1M-0.1mM)	2.0×10^{13}	7.0